



Dynamics of **endo**- vs. **exo**-complexation and electronic absorption of calix[4]arene-Ar₂



Benedito J.C. Cabral ^{a,b,c,*}, Kaline Coutinho ^c, Sylvio Canuto ^c

^a Grupo de Física Matemática da Universidade de Lisboa, Av. Professor Gama Pinto 2, 1649-003 Lisboa, Portugal

^b Departamento de Química e Bioquímica, Faculdade de Ciências, Universidade de Lisboa, 1749-016 Lisboa, Portugal

^c Instituto de Física da Universidade de São Paulo, CP 66318, 05314-970 São Paulo, SP, Brazil

ARTICLE INFO

Article history:

Received 11 July 2014

In final form 13 August 2014

Available online 19 August 2014

ABSTRACT

The dynamics of the calix[4]arene cone conformer (cax[4]) and calix[4]arene-Ar₂ complexes (cax[4]-Ar₂) at three temperatures ($T = 20, 100$, and 200 K) was investigated through Born–Oppenheimer molecular dynamics (BOMD). Thermal effects on the *endo*- vs. *exo*-complexation dynamics, the vibrational dynamics of the homodromic OH bond array, and the electronic absorption spectra are investigated. In comparison with results for the electronic spectra of gas-phase optimized structures, thermal effects on the electronic absorption spectra lead to a red-shift and broadening of the low energy excitation maxima.

© 2014 Elsevier B.V. All rights reserved.

1. Introduction

Calix[n]arene supramolecular structures [1–3] play a central role in molecular recognition. The calix[n]arene structures are defined by a cyclic phenolic array of variable size linked by [n] methylene groups. They are easily functionalized structures both at the top rim (methylene groups) as well as at the bottom rim that corresponds to a cyclic array of OH groups energetically stabilized by intramolecular homodromic hydrogen bonds (HB) [4,5]. The definition of an HB array as homodromic stresses the feature that all the HB have a unique orientation relative to a reference axis [4]. Cooperative polarization effects play an important role on the energetics and dynamics of hydrogen bonds and it is expected that these effects are even stronger in homodromic HB arrays [4,5]. Calix[n]arenes are also characterized by the presence of a cavity with a delocalized π electronic distribution of the phenyl rings. This cavity is able to strongly interact with a diversity of molecular species including charged species (anions and cations) [6,7] as well as with small molecules [8–10]. The design and synthesis of supramolecular structures with selective binding abilities is of fundamental importance for materials science [11–14], medical [15] and biochemical applications [16,17]. Selective binding is related to specific interactions between a host (usually a supramolecular structure) and a guest species. Host–guest interactions in calix[n]arenes are determined by non-additive cooperative effects associated with the π electron distribution in the internal cavity.

Complexation of charged species with calix[n]arenes is driven by cation– π interactions [6,18,19,20]. Encapsulation by calix[n]arene of a variety of neutral guest species including rare-gas atoms and small molecules (CH₂, N₂, C₂H₂) [10] is driven by dispersion interactions between these species and the π electronic distribution of the host [13,21]. Complexation with small polar molecules including H₂O and NH₃ [10] and CH₃Cl [8] illustrates the role played by dipole– π interactions.

A reference system in nanotechnology is calix[4]arene (cax[4]) that is present in four different conformers such as the cone, partial cone, 1,2-alternate, and 1,3-alternate [22]. For several species, the interaction with the calix[4]arene host may lead to the formation of *endo*- or *exo*- complexes [9,10]. The host–guest energetics and dynamics is of particular interest when more than one single guest species is present. In this case the dynamics of *endo*- vs. *exo*-complexation is also coupled to the guest–guest interactions. This is the case of calix[4]arenes-Ar_n complexes for which experimental data on the vibrational spectra are available [9]. A central issue concerning the complexation of cax[4] with small van der Waals species is the formation of *endo*- or *exo*-complexes [9]. NMR or X-ray diffraction data on the structure of these systems normally rely on experiments carried out at room temperature [10]. At high temperatures thermal energies become comparable with host–guest interactions and the interpretation of experimental data is difficult due to thermal broadening [10]. Several works were dedicated to study the van der Waals complexes of small molecules with calix[4]arenes [9,10,23,24]. The dynamics of complexation of a related system (*pert-tertbutyl-calix[4]arene*) with small species including H₂, CO₂ and Xe was also the subject of different works [25,26]. These previous studies were carried out

* Corresponding author at: Grupo de Física Matemática da Universidade de Lisboa, Av. Professor Gama Pinto 2, 1649-003 Lisboa, Portugal.

with classical molecular dynamics [25]. A correct description of dispersion interactions is essential to investigate the structure and electronic properties of calix[n]arenes interacting with van der Waals species. Theoretical progress in the description of dispersion interactions has been accomplished by including empirical corrections for the dispersion interaction energy in density functional theory (DFT) methods [27–29]. DFT methods with empirical corrections to dispersion interactions can be applied to large supramolecular complexes [29].

In this work we investigate the dynamics of calix[4]arene ($\text{cax}[4]$) and calix[4]arene- Ar_2 ($\text{cax}[4]\text{-Ar}_2$) complexes with two main purposes. The first one concerns the analysis of thermal effects on the *endo*- vs. *exo*-complexation dynamics, and the vibrational dynamics of the homodromic hydrogen bond array at the $\text{cax}[4]$ lower rim. The second purpose is focused on the electronic absorption spectra and their dependence with the temperature. The presently adopted theoretical approach relies on Born–Oppenheimer molecular dynamics (BOMD) [30] and time dependent density functional theory (TDDFT) [31]. The Letter is organized as follows. Initially, the theoretical procedures are described. This is followed by a discussion on the structure, binding energies, and electronic spectra of gas-phase optimized structures. The dynamics of calix[4]arene- Ar_2 at different temperatures is then analysed with emphasis on the dynamics of the homodromic hydrogen bond array at the $\text{cax}[4]$ lower rim and on the dependence of the *endo*- vs. *exo*-complexation with the temperature. The last section analyses thermal effects on the electronic absorption spectra of $\text{cax}[4]$ and $\text{cax}[4]\text{-Ar}_2$ systems.

2. Computational details

Geometry optimizations for $\text{cax}[4]$ and $\text{cax}[4]\text{-Ar}_2$ complexes were carried out with the CP2K program [32]. The hybrid Gaussian and plane-wave method GPW [33] as implemented in the QUICK-STEP module [32] was adopted. Goedecker, Teter, and Hutter (GTH) norm-conserving pseudopotentials [34] were used for representing the core electrons and only valence electrons were explicitly included in the quantum mechanical density functional theory (DFT) calculations for the geometry optimizations and BOMD. DFT calculations were carried with the Perdew–Burke–Ernzerhof (PBE) exchange-correlation functional [35] (the PBE calculations with the GTH pseudopotentials will be represented as PBE[GTH]). An empirical correction to dispersion interactions (D3) proposed by Grimme et al [28] was added to the PBE functional for the geometry optimizations and BOMD. This method will be represented as PBE[GTH]-D3. We adopted the GPW approach, where Kohn–Sham orbitals are expanded into atom-centered triple-zeta-valence-polarization (TZVP) Gaussian-type orbital functions, whereas the electron density is represented with an auxiliary plane-wave basis-set. A charge density cutoff of 280 Ry was used for the auxiliary basis-set and the self-consistent-field energy threshold for calculating the electronic density was 10^{-7} Hartree. Geometry optimizations and BOMD were carried in a cubic cell of 22 Å. Non-periodic boundary conditions with the Martyna–Tuckerman Poisson solver [36] were adopted.

BOMD [30] was performed in the (NVT) canonical ensemble with a canonical sampling through velocity rescaling (CSVN) thermostat [37] and target temperatures of 20, 100, and 200 K. A timestep of 0.25 fs was used. The total time of the BOMD run was 12.5 ps (50 000 steps). The final average temperatures deviate less than 2 K from the targeted ones and the largest value of the standard deviation is ± 3 K. Therefore, reference will be made only to the target values.

The configurations from the last 8 ps of BOMD were used for the analysis of the structure, dynamics, vibrational, and electronic

properties. A total of 400 configurations (equally separated in time) were selected for the analysis of the electronic absorption spectra. Excitation energies were calculated with TDDFT [31]. The number of excited states (N_s) was 50 for each selected configuration. The excitation energies were calculated with the ORCA program [38]. Data for the excitation energies and oscillator strengths were convoluted by a Lorentzian distribution of 0.10 eV width. The PBE-D3 functional and the Ahlrichs TZVP basis-set [39] were adopted for TDDFT calculations. However, TDDFT calculations were performed with all the electrons and this approach will be represented as PBE-D3. For comparison, additional geometry optimizations of $\text{cax}[4]$ and $\text{cax}[4]\text{-Ar}_2$ complexes were also carried out with this same approach.

3. Results and discussion

3.1. Optimized structures, binding energies, and gas-phase electronic absorption spectra

3.1.1. Optimized structures

Optimized structures for the cone conformer of calix[4]arene and their *endo*- and *exo*-complexes are shown in Figure 1. In agreement with experimental [40] and theoretical [41] works the $\text{cax}[4]$ cone conformer has a C_4 symmetry axis. The *endo*- $\text{cax}[4]\text{-Ar}_2$ or 2:0 complex is characterized by the inclusion of the Ar_2 molecule in the $\text{cax}[4]$ cavity. In the *exo*- $\text{cax}[4]\text{-Ar}_2$ or 1:1 complex one Ar atom is inside the cavity, whereas the second one is outside the macrocycle and interacts with one of the phenyl fragments. The structure of $\text{cax}[4]\text{-Ar}_2$ complexes can be discussed by defining two additional coordinates. The first (X_1) is the center-of-mass (c.o.m.) of the macrocycle (Ar atoms are not included). The second (X_2) is the c.o.m. of the oxygen atoms at the $\text{cax}[4]$ lower rim. The C_4 symmetry axis of the gas-phase optimized $\text{cax}[4]$ structure coincides with the $X_2\text{-}X_1$ axis (see Figure 1). For clarity the Ar atom more distant from the $\text{cax}[4]$ c.o.m. (X_1) is represented by Ar' .

Some geometric parameters for $\text{cax}[4]\text{-Ar}_2$ are gathered in Table 1. For the *endo*- $\text{cax}[4]\text{-Ar}_2$ complex the $\text{Ar}\text{-Ar}'$ distance ($d[\text{Ar}\text{-Ar}']$) for the optimized geometry at the PBE-D3[GTH]/TZVP level is 3.89 Å. The distances between the Ar atoms and the $\text{cax}[4]$ center-of-mass are 2.10 Å and 5.37 Å for Ar ($d[\text{Ar-X}_1]$) and Ar' ($d[\text{Ar}'\text{-X}_1]$), respectively. The Ar atom is on the $\text{cax}[4]$ C_4 symmetry axis and the angle between this axis and the Ar' atom ($\angle[X_1\text{-Ar}\text{-Ar}']$) is 124.5 degrees. For *exo*- $\text{cax}[4]\text{-Ar}_2$ the distance between the Ar atom inside the cavity and $\text{cax}[4]$ center-of-mass ($d[\text{Ar-X}_1]$) is 2.06 Å. The Ar' atom is outside the $\text{cax}[4]$ cavity, $d[\text{Ar}\text{-Ar}']$ is 7.4 Å, and $d[\text{Ar}'\text{-X}_1]$ is 6.6 Å. Therefore, the $\text{Ar}\text{-Ar}$ bond is broken in the optimized structure of the *exo*- $\text{cax}[4]\text{-Ar}_2$ complex. The angle between the C_4 axis and the Ar' ($\angle[X_2\text{-X}_1\text{-Ar}']$) atom is 74 degrees. Results for geometry optimizations relying on all-electron calculations are also presented in Table 1. A reasonable agreement between pseudopotentials and all-electron calculations for the geometry of $\text{cax}[4]\text{-Ar}_2$ complexes is observed. It should be also noticed that PBE-D3[GTH]/TZVP calculation predicts that the gas-phase Ar_2 equilibrium distance is 3.75 Å, which is in very good agreement with the reference value for the isolated Ar_2 molecule (3.758 Å) [42]. At the PBE-D3[GTH]/TZVP level, the binding energy of the Ar_2 system with correction to the basis set superposition error is 108 cm⁻¹, which is only 8.5 cm⁻¹ above the value reported by Aziz (99.5 cm⁻¹) [42].

3.1.2. Binding energies

Binding energies of $\text{cax}[4]$ with different species including rare gas systems have been investigated by several works [9,10]. Here, our main purpose is to assess the adequacy of the presently adopted theoretical approach relying on the inclusion of an empirical

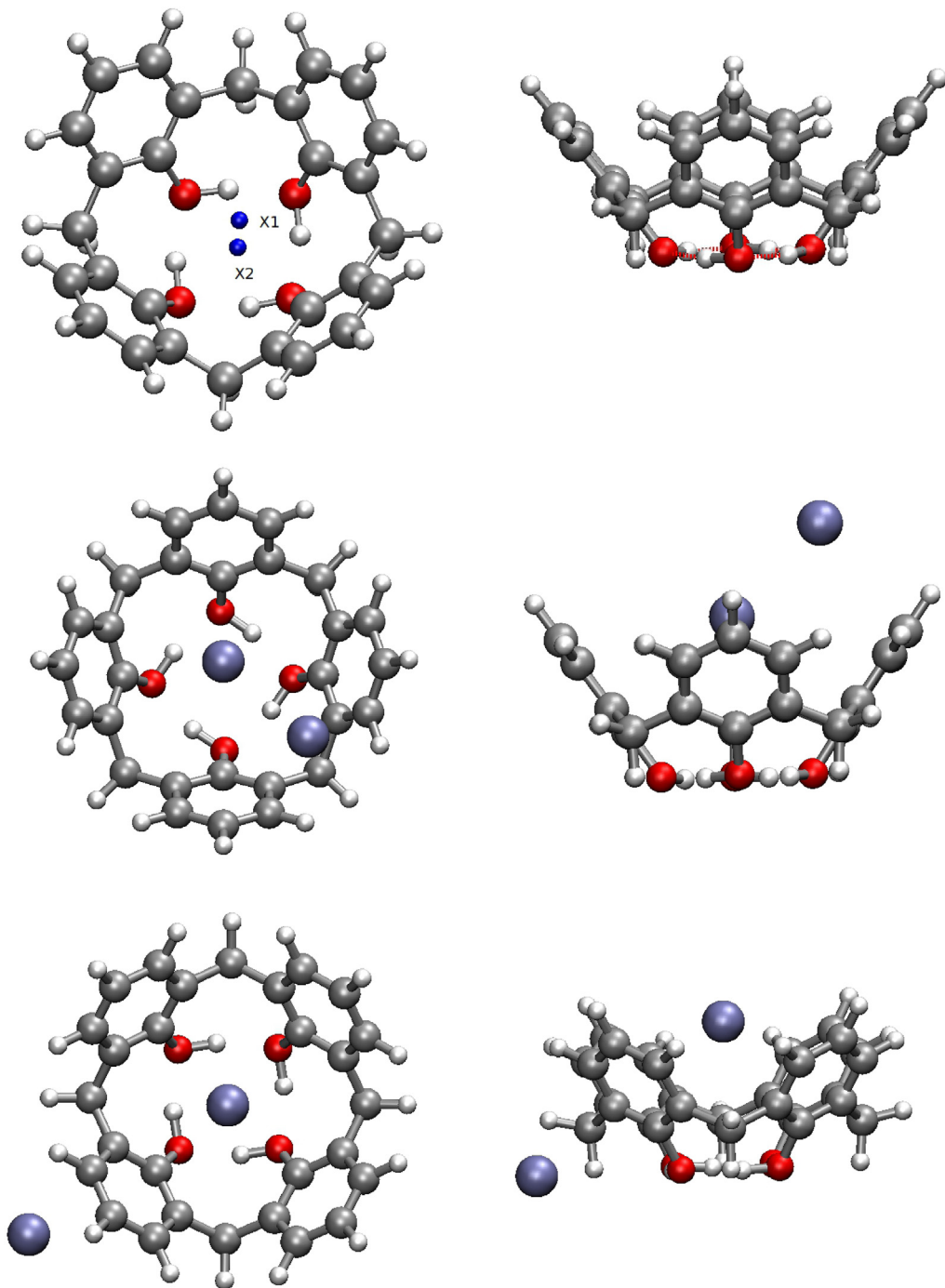


Figure 1. Optimized structures of calix[4]arene (cax[4]) and cax[4]-Ar₂ complexes. Upper panel: cax[4]; center: *endo*-cax[4]-Ar₂; bottom: *exo*-cax[4]-Ar₂. Top view (left) and side view (right). The center of mass of cax[4] is represented by X₁. The center of mass of the oxygen atoms is represented by X₂. The X₂-X₁ axis is the C₄ symmetry axis of cax[4].

correction to the dispersion energy in DFT [27,28] to describe the host-guest interactions. We will focus the discussion on the binding energy (BE) of cax[4]-Ar system for which theoretical and experimental data is available [9]. The theoretical calculations include corrections to the basis-set superposition error. Fragment relaxation and zero-point vibrational energies were not taken into account. The calculations were performed with PBE[GTH]-D3/TZVP optimized geometries. The binding energy (BE) of the *endo*-cax[4]-Ar complex predicted by PBE[GTH]-D3/TZVP is 1374 cm⁻¹. An all-electron calculation at the PBE-D3/TZVP level leads to 1310 cm⁻¹. Theoretical results relying on MP2 and CCSD(T)

are in the ~1000–2200 cm⁻¹ range [9], whereas CCSD(T) calculations lead to significantly lower values, which are close to 1000 cm⁻¹ [9]. The experimental value for the BE of the cax[4]-Ar system is in a wide range (350–2250 cm⁻¹) [9].

The reliability of the proposed approaches to describe dispersion interactions through the inclusion of empirical corrections is a subject under debate in the literature [43]. However, the agreement between BEs predicted by PBE-D3[GTH], *ab initio* results [9], and experimental information [9] is an indication on the adequacy of the presently adopted approach to carry out BOMD for the cax[4]-Ar₂ system.

Table 1

Geometric data for the gas-phase optimized structures of cax[4]-Ar₂ complexes and averages values from BOMD at different temperatures (in K). Distances in Å. Angles in degrees. Geometry optimizations and BOMD carried out at the PBE-D3(GTH)/TZVP level. Values in parentheses for optimized structures are all electron PBE-D3/TZVP calculations.

	<i>endo</i> -cax[4]-Ar ₂	<i>exo</i> -cax[4]-Ar ₂	
Optimized structures			
d[Ar-Ar']	3.89 (3.80)	7.40 (7.25)	
d[Ar-X ₁]	2.10 (2.01)	2.06 (2.04)	
d[Ar'-X ₁]	5.37 (5.26)	6.6 (6.28)	
∠[X ₂ -X ₁ -Ar]	180.0 (180.0)	180.0 (180.0)	
∠[X ₂ -X ₁ -Ar']	144.0 (144.9)	74.0 (69.1)	
∠[X ₁ -Ar-Ar']	124.6 (126.7)	58.6 (54.3)	
Average values from BOMD			
T	20	100	200
d[Ar-Ar']	4.1 ± 0.4	6.9 ± 2	6.2 ± 2
d[Ar-X ₁]	2.7 ± 0.8	5.4 ± 1.5	7.2 ± 1
d[Ar'-X ₁]	5.5 ± 0.5	8.7 ± 0.5	9.3 ± 0.5
∠[X ₂ -X ₁ -Ar]	174 ± 4	149 ± 11	143 ± 12
∠[X ₁ -Ar-Ar']	122 ± 7	92 ± 23	92 ± 22

3.1.3. Electronic absorption spectra

For the gas-phase optimized structure of cax[4] four maxima in the electronic absorption spectrum are predicted at $\lambda = 308$, 293, 259, and 240 nm, respectively. Experimental results in liquid methanol [44] predict peak positions at $\lambda = 282$, 274, and 262 nm. In addition, a broad band in the 220–230 nm is also reported [44]. The reported peak positions for *p*-tert-butyl calix[4]arene in dimethylformamide (DMF) [45] are at $\lambda = 318$, 288, and 262 nm. TDDFT PBE-D3/TZVP results for the first three peak positions are in good agreement with the experimental data for *p*-tert-butyl calix[4]arene in dimethylformamide (DMF) [45] with a maximum deviation of 10 nm. In agreement with the results by Boo et al. [44] the calculated electronic absorption spectrum of cax[4] also shows a maximum at 240 nm, which is in good agreement with a broad band that peaks in the 220–230 nm region. The simulated electronic absorption spectra for the optimized structures of cax[4] and cax[4]-Ar₂ complexes are shown in Figure 2. Minor differences are observed between the spectra for the optimized structures of cax[4] and cax[4]-Ar₂. In comparison with cax[4] and *exo*-cax[4]-Ar₂ the high energy peak of *endo*-cax[4]-Ar₂ is slightly blue-shifted; for both cax[4]-Ar₂ complexes a low-energy tail peaked at ~310 nm is red-shifted relative to cax[4].

Although a direct comparison between the experimental data and theoretical results for gas-phase optimized structure is limited due to solvent effects the present agreement between our theoretical results and experiment supports the choice of TDDFT

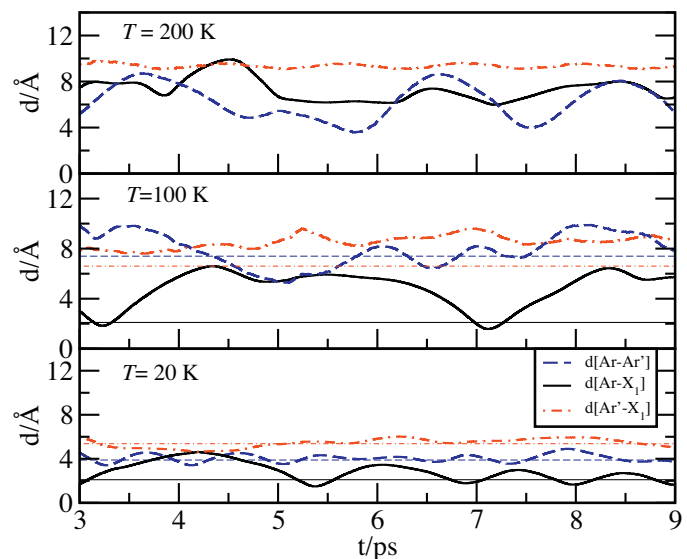


Figure 3. Time evolution of reference distances (see text) for different temperatures. d[Ar-X₁] and d[Ar'-X₁] are the distances between the cax[4] c.o.m and the Ar atoms. d[Ar-Ar'] is the distance between the argon atoms. The horizontal lines for T=20 K and T=100 K represent the distances for the gas-phase *endo*- and *exo*-optimized structures, respectively (see Table 1). Distances in Å.

PBE-D3/TZVP to predict electronic excitation energies for the systems of interest. The same method will be applied to calculate the absorption spectra at different temperatures using selected configurations generated by BOMD.

3.2. Thermal effects on the dynamics and electronic absorption of cax[4]-Ar₂

3.2.1. Temperature dependent *endo*- vs. *exo*-complexation

Thermal effects on the dynamics of the cax[4]-Ar₂ system can be investigated by analysing the time evolution of some specific parameters at different temperatures. The present analysis will be initially focused on the time evolution of the distance between the nearest Ar atom and the cax[4] c.o.m (X_1) (d[Ar-X₁]), the second Ar atom and X_1 (d[Ar'-X₁]), and the distance between the Ar atoms (d[Ar-Ar']). These parameters allows us to follow the dynamics of the Ar atoms in interaction with the cax[4] macrocycle. The time evolution of these distances is presented in Figure 3 and the average values for different temperatures are reported in Table 1. For the lower temperature (T=20 K) the time evolution of d[Ar-X₁] and d[Ar'-X₁] indicates that the two atoms are inside the cax[4] cavity. The average values of these two distances are 2.7 ± 0.8 Å and 5.5 ± 0.5 Å, respectively. In addition, the average of d[Ar-Ar'] is 4.1 ± 0.4 Å, which is close to the value for the optimized geometry of the *endo*-complex (3.9 Å). Further evidence on *endo*- complexation at this temperature is provided by the average values for the ∠[X₂-X₁-Ar] and ∠[X₁-Ar-Ar'] angles (see Table 1). The average values of ∠[X₂-X₁-Ar] and ∠[X₁-Ar-Ar'] are 174 ± 4 and 122 ± 7 degrees, quite close to the values for the gas-phase optimized *endo*-cax[4]-Ar₂ complex, which are 180.0 and 124.5 degrees, respectively.

The dynamics at T=100 K is illustrated in the middle panel of Figure 3. The time evolution of d[Ar-X₁] shows that this distance is roughly distributed in a 2–6 Å interval with an average value of 5.4 ± 1.5 Å, whereas a second Ar' atom is outside the cax[4] cavity with an average d[Ar'-X₁] distance of 8.7 ± 0.5 Å. The average d[Ar-Ar'] is 6.9 ± 2 Å, which can be compared to the distance for the gas-phase optimized *exo*-cax[4]-Ar₂ complex (7.4 Å). A broad distribution of the ∠[X₂-X₁-Ar] and ∠[X₁-Ar-Ar'] angles is observed at

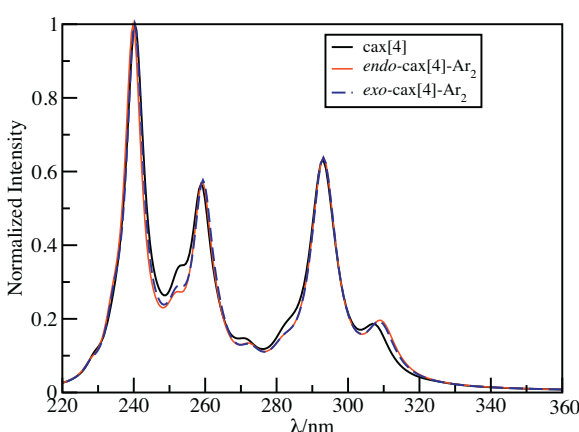


Figure 2. Excitation spectra for the optimized structures of cax[4] and cax[4]-Ar₂ *exo*- and *endo*- complexes. PBE-D3/TZVP calculations.

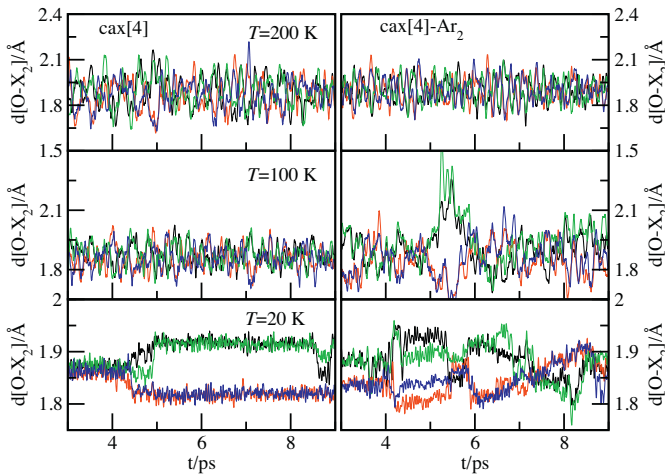


Figure 4. Time evolution of the distance $d[O-X_2]$ between each oxygen atom and the c.o.m. of the oxygen atoms X_2 for cax[4] (left) and cax[4]-Ar₂ (right) at different temperatures. The oxygen atoms associated with the black and red (or green and blue) curves belong to face-to-face phenol rings. (For interpretation of the references to color in this legend, the reader is referred to the web version of the article.)

$T = 100\text{ K}$. Their average values are 149 ± 11 and 92 ± 23 degrees. The average value of $\angle[X_2-X_1-\text{Ar}]$ indicates a deviation of the nearest Ar atom from the central axis of the cax[4] cavity that corresponds to a C_4 axis for the gas-phase optimized structure. The lowest $\angle[X_1-\text{Ar}-\text{Ar}']$ values are close to the optimized value for the *exo*-cax[4] complex (~ 59 degrees). Although most of the time both Ar atoms are outside the macrocycle cavity, the cax[4]-Ar₂ dynamics at $T = 100\text{ K}$ is in keeping with an *exo*-cax[4]Ar₂ complexation scenario associated with a broad distribution of some reference geometric parameters.

The time evolution of the defined geometric parameters for the cax[4]-Ar₂ system at $T = 200\text{ K}$ is also illustrated in Figure 3. In this case both Ar atoms are outside the cax[4] cavity. The average values of $d[\text{Ar}-X_1]$ and $d[\text{Ar}'-X_1]$ are $7.2 \pm 1\text{ \AA}$ and $9.3 \pm 0.5\text{ \AA}$, respectively. The average $d[\text{Ar}-\text{Ar}']$ is $6.2 \pm 2\text{ \AA}$ and the time evolution of this distance (see Figure 3) suggests Ar–Ar' bond formation and breaking. The average values of $\angle[X_2-X_1-\text{Ar}]$ and $\angle[X_1-\text{Ar}-\text{Ar}']$ are 143 ± 12 and 92 ± 22 degrees, respectively. These values are similar to those observed at $T = 100\text{ K}$ (see Table 1).

Figure 4 presents for cax[4] (left panels) and cax[4]-Ar₂ (right panels), and for different temperatures, the time evolution of the distances between each oxygen atom and their center-of-mass (X_2) that is represented by ($d[O-X_2]$). Although X_2 is determined by the oxygen atoms position, the distribution of the O-X₂ distances at a temperature T may give us an indication on the changes of the cax[4] structure relative to the gas-phase optimized geometry. For cax[4] the dynamics of $d[O-X_2]$ at $T = 20\text{ K}$ shows, for a $\sim 4\text{ ps}$ time window, two oxygen atoms belonging to face-to-face phenyl units at an average distance of $1.89 \pm 0.02\text{ \AA}$ from X_2 , whereas the other two atoms are closer to X_2 at an average distance of $1.83 \pm 0.02\text{ \AA}$. Due to thermal effects, it should be expected that the C_4 symmetry of the gas-phase optimized cax[4] is broken at a finite temperature T . However, the present geometric pattern seems to be in keeping with the presence of a nearly C_2 symmetric structure at $T = 20\text{ K}$. Further evidence of a nearly C_2 symmetry is provided by the calculation of the average distances between two oxygen atoms belonging to opposite phenol moieties. The average values are $3.66 \pm 0.03\text{ \AA}$ and $3.79 \pm 0.04\text{ \AA}$, whereas average values for the distances between adjacent oxygen atoms are quite similar ($2.63 - 2.64 \pm 0.02\text{ \AA}$). It should be noticed that the average distances between carbon atoms of opposite methylene groups are identical ($7.24 \pm 0.01\text{ \AA}$).

and coincide with the values for the gas-phase optimized structure. Therefore, the size of the cax[4] upper rim is not modified at $T = 20\text{ K}$.

$C_4 \leftrightarrow C_2$ symmetry transitions in calix[n]arenes are usually related to interactions with ionic or molecular species [2] or with a solvent [46]. These interactions influence the O–H...O structure at the lower rim and lead to significant differences on the OH stretch frequency in different solvents such as CCl_4 and CS_2 [46].

A more complex pattern is observed for cax[4]-Ar₂ at $T = 20\text{ K}$. In this case, four distances are defined although two pairs of similar distances belonging to face-to-face phenyl units can be identified. This situation corresponds to an *endo*-cax[4]-Ar₂ complexation scenario and reflects additional distortions of the cax[4] macrocycle due to host–guest interactions. The distortions are, as expected, associated with the position of the Ar atom inside the cax[4] cavity. The sudden changes of $d[O-X_2]$ for $t = \sim 5.5, 7$ and 8 ps (Figure 4) are correlated with the position of the Ar atom that approaches the cax[4] c.o.m. (X_1) nearly at the same times (see bottom panel of Figure 3).

For cax[4] at the higher temperatures (100 K and 200 K), the average $d[O-X_2]$ distances are similar. However, significant fluctuations of $d[O-X_2]$ are observed for cax[4]-Ar₂ at $T = 100\text{ K}$. This feature seems to be related to the dynamics of the Ar atoms interacting with cax[4] in a system that exhibits some structural similarities with an *exo*-cax[4]-Ar₂ complex. The time evolution of $d[O-X_2]$ at $T = 200\text{ K}$ for both cax[4] and cax[4]-Ar₂ shows similar patterns and reflects, essentially, the distortions of the host structure induced by thermal effects. As illustrated in Figure 3 (top panel) both Ar atoms are outside the cax[4] cavity at this temperature.

3.2.2. Dynamics of the homodromic OH...O hydrogen bond array

The cax[4] lower rim is characterized by the formation of an intramolecular hydrogen bond (HB) array involving the OH group of the phenyl moieties. The uni-directional OH...O HB array is called homodromic [4] to stress the feature that all the hydrogen bonds have a unique orientation, which is presently clockwise relative to the central X_2-X_1 axis. An interesting aspect concerning the cax[4] dynamics is the reversal of the OH vibrational motion of the OH bond array that was observed by Lang et al. [47] in the temperature range of 221–304 K. Although the present results for the dynamics of the OH bond array at the higher temperatures ($T = 100\text{ K}$ and $T = 200\text{ K}$) is in keeping with the experimental assignment of four equivalent hydrogen bonds for cax[4] [47] no reversal of the HB array was observed. It should be noticed, however, that the concerted reversal of the OH motion at the homodromic array is very dependent on the temperature and that it was not experimentally detected for temperatures below $\sim 220\text{ K}$ [47]. Moreover, the flip-flop rates are in the order of $10^2 - 10^4\text{ s}^{-1}$ [47], and therefore the concerted reversal of the HB array is not accessible to a 12 ps molecular dynamics run.

A fingerprint of HB formation involving the OH group is the red-shift of the O–H stretching frequency relative to the situation where there is no HB. This frequency shift can be related to the stretching of the O–H bond relative to a reference value. The distribution of the $\nu(\text{O–H})$ stretching frequency can be analysed by calculating the Fourier transform of the average velocity autocorrelation function defined as $C_{AA}(t) = \langle A(t)A(t_i)/A(t_i)A(t_i) \rangle$ where $A = dx/dt$, t_i a time origin, and $x = d(\text{O–H})$. A similar procedure was recently applied to calculate the vibrational frequencies of chlorophyll- c_2 in liquid methanol [48]. The high value of the $\nu(\text{O–H})$ stretching frequency ($\sim 3000\text{ cm}^{-1}$) contributes to the convergence of the velocity autocorrelation function and a good estimate of $C_{AA}(t)$ is possible by using the data from the total production time (8.5 ps) of the present BOMD.

Figure 5 presents the $\nu(\text{O–H})$ frequency distribution for cax[4] and cax[4]-Ar₂ at different temperatures. For the lower temperature ($T = 20\text{ K}$) and for the cax[4] system, the distribution shows

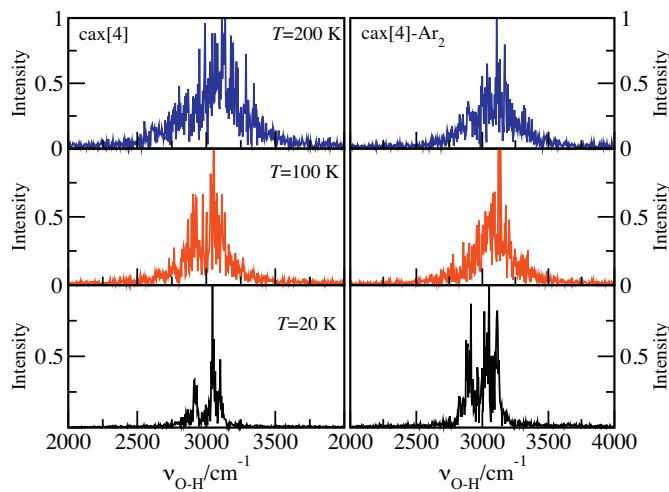


Figure 5. O–H vibrational distribution in cax[4] (left) and cax[4]–Ar₂ (right) at different temperatures.

a bimodal distribution with peaks at 2930 and 3060 cm⁻¹. The bimodal distribution seems to reflect the presence of two different HB interactions related to the structure and dynamics of the cax[4] macrocycle and the OH array at the lower rim. This feature, which is a characteristic of the lower temperature, is not observed at the higher temperatures (100 K and 200 K). Experimental data by Kovalenko et al. [49] for cax[4] in a CCl₄ solution shows a single $\nu(O-H)$ frequency maximum at 3173 cm⁻¹. However, the same authors pointed out that a bimodal distribution is observed in the vibrational spectrum of crystalline cax[4] with a doublet contour at 3247/3147 cm⁻¹. The presence of two nonequivalent O–O distances in the crystalline phase was invoked to explain the bimodal distribution [49].

The $\nu(O-H)$ frequency distribution for the cax[4]–Ar₂ systems are also presented in Figure 5 (right panels). For T=20 K, the distribution shows a maximum at ~3100 cm⁻¹, which is in good agreement with the value predicted by jet-cooling experiments on cax[4]–Ar (3160 cm⁻¹) [10]. The $\nu(O-H)$ frequency distributions are slightly blue-shifted with increasing temperature. This blue-shift with increasing temperature is related to structural distortions at the cax[4] lower rim and with a consequent weakening of the homodromic OH bonds. For the cax[4] system at T=20 K, Figure 6 presents the N|∠HOO distribution of ∠HOO that is defined as the angle between the HO bond vector and the vector from the O oxygen to the oxygen atom at the opposite (face-to-face) phenol ring. The value of this angle for the optimized gas-phase structure (C_4 symmetry) is 54.0 degrees. The two first distributions (Ia and Ib) correspond to an average distance between opposite oxygen atoms of 3.79 ± 0.04 Å. For the other two distributions (IIa and IIb) the average oxygen–oxygen distance is 3.66 ± 0.03 Å. The average values of ∠HOO are 52.6 ± 1.4 degrees and 54.4 ± 1.3 degrees for distributions I and II, respectively. The results indicate two different orientations of the OH group relative to the OH···O bond depending on the position of the oxygen atoms at the cax[4] lower rim. Consequently, two slightly different groups of equivalent HBs can be defined. The first group (Ia and Ib) corresponds to a weaker HB associated with a greater deviation from linearity, and an increased OH···O bond distance. These differences are at the origin of the $\nu(O-H)$ red shift of the first group (Ia and Ib) relative to the second one (IIa and IIb). Although the effect is small the N|∠HOO distribution provides further evidence on the structural features characterizing cax[4] at T=20 K and supports the analysis of the data for the vibrational spectrum.

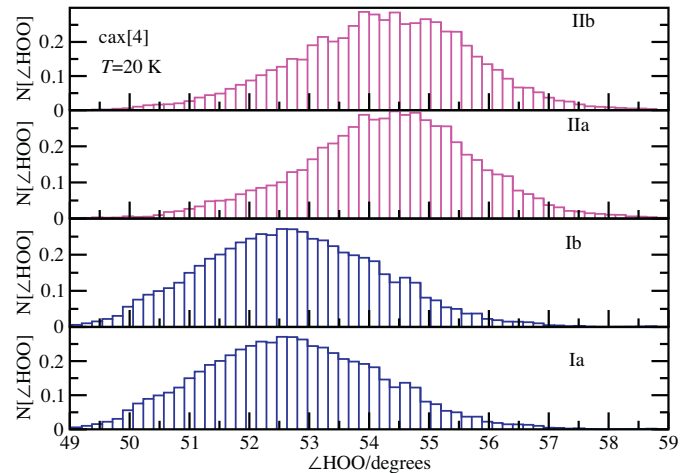


Figure 6. Distribution of the ∠HOO angle (see text) for each OH group of cax[4] at T=20 K. The distributions Ia and Ib correspond to OH groups attached to face-to-face phenyl units with an average oxygen–oxygen distance of 3.79 ± 0.04 Å. For IIa and IIb this average distance is 3.66 ± 0.03 Å.

3.2.3. Thermal effects on the electronic spectra of cax[4] and cax[4]–Ar₂

The electronic spectra of cax[4] and cax[4]–Ar₂ are presented in Figure 7. For cax[4], the lower energy absorption peak at $\lambda = 293$ nm for the optimized structure is red-shifted by 6–8 nm at T=100 and 200 K. A broadening of the lower energy absorption tail is also observed. High energy excitations are not very dependent on T and only small red-shifts relative to the optimized structures are observed. Comparison between the results for cax[4] at the different temperatures and experiment shows a good agreement with experimental data, particularly for the case of cax[4] in formaldehyde [45]. In comparison with the spectrum for the optimized structures the absorption spectra of cax[4]–Ar₂ at T=20 and 100 K are not modified. Only for T=200 K a ~5–7 nm red-shift of the peak positions is observed. Comparison between the cax[4] and cax[4]–Ar₂ spectra shows that they are quite similar. In the first two cases (T=20 and 100 K) the results indicate that endo- or exo- complexation of cax[4] with Ar₂ does not change, in a significant way, the electronic absorption spectrum in comparison with cax[4]. For the highest temperature (T=200 K), the results reflect the feature that Ar₂ is outside the cax[4] macrocycle and

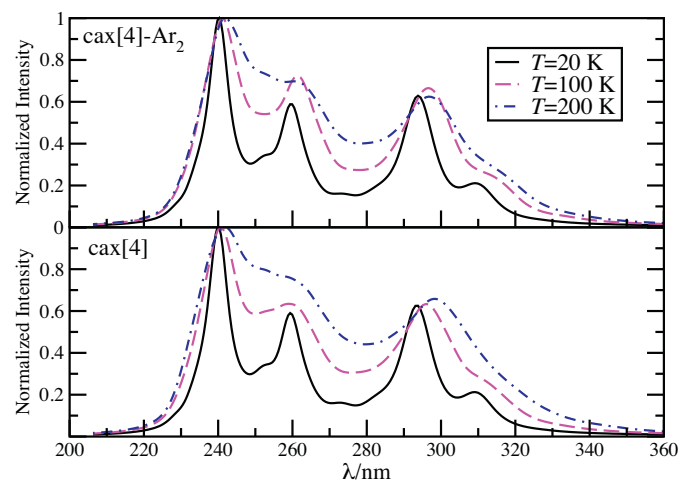


Figure 7. Electronic absorption spectra of cax[4] and cax[4]–Ar₂ at different temperatures. Lower panel (cax[4]); higher panel (cax[4]–Ar₂). TDDFT excitation energies (in nm) from PBE-D3/TZVP calculations.

the absorption spectrum should be quite similar to that one of cax[4].

4. Conclusions

Born–Oppenheimer molecular dynamics (BOMD) for cax[4] and cax[4]–Ar₂ were carried out and provided fundamental information to understand the role played by thermal effects on the dynamics, vibrational and electronic properties of these systems. For cax[4] the results indicate that nearly C₂ symmetric structures are present at T=20 K. A thermally induced C₄ (gas-phase optimized cax[4]) to C₂ (BOMD generated structures at T=20 K) symmetry transition is observed. The analysis of the structure of cax[4] at T=20 K strongly indicates the presence of two nonequivalent oxygen–oxygen distances at the cax[4] lower rim. A fingerprint of the presence of these configurations is a bimodal distribution of the ν(O–H) stretching vibrational frequencies that is characteristic of cax[4] at the low temperature of 20 K. A blue-shift of the ν(O–H) vibrational frequencies of the cax[4] homodromic array with increasing temperature was also observed. The dynamics of the cax[4]–Ar₂ system is temperature dependent and the results strongly indicate that at T=20 K only an *endo*-cax[4]–Ar₂ system is observed. The data for T=100 K is compatible sometimes with a picture of *exo*-complexation where one Ar atom is inside the cax[4] cavity, whereas a second one is outside. A T=200 K, a cax[4]–Ar₂ structure where both Ar atoms are outside the cax[4] cavity was found. The results for this temperature also suggest the eventual formation of an *exo*-Ar₂ diatomic species interacting with the cax[4] macrocycle. Time dependent density functional theory calculations (TDDFT) for cax[4] and cax[4]–Ar₂ systems were also carried out. Results for the gas-phase optimized structures and averages over configurations generated by BOMD at the different temperatures were compared. The main effect of temperature on the electronic absorption spectrum of cax[4] concerns the low-energy absorption region above 280 nm that shows a ~8–10 nm red-shift of the peak positions and broadening of the low-energy absorption tails. Comparison between the electronic absorption spectra of cax[4] and cax[4]–Ar₂ at different temperatures indicate that they are quite similar.

Acknowledgements

Work partially supported by FCT (Portugal), CNPq, CAPES, FAPESP, INCT-FCx and nBioNet (Brazil). BJCC gratefully acknowledges support from the Universidade de São Paulo through a research grant. The authors would like to thank Vinicius W. D. Cruzeiro for helpful discussions.

References

- [1] A. Ikeda, S. Shinkai, Chem. Rev. 97 (1997) 1713.
- [2] C.D. Gutsche, Calixarenes revisited, in: J. Fraser Stoddart (Ed.), *Monographs in Supramolecular Chemistry*, Royal Society of Chemistry, Cambridge, 1998.
- [3] C.D. Gutsche, Calixarenes: an overview, in: J.L. Atwood, J.E.D. Davies, D. Mac-Nicol (Eds.), *Inclusion Compounds*, Oxford University Press, Oxford, 1991, p. 27.
- [4] W. Saenger, et al., Proc. Int. Symp. Biomol. Struct. Interact. Suppl. J. Biosci. 8 (1985) 437.
- [5] S.S. Xantheas, Chem. Phys. 258 (2000) 225.
- [6] D.A. Dougherty, Science 271 (1996) 163.
- [7] D.-X. Wang, M.-X. Wang, J. Am. Chem. Soc. 135 (2013) 892.
- [8] F. Benevelli, A. Bond, M. Duer, J. Klinowski, PhysChemChemPhys 2 (2000) 3977.
- [9] T. Ebata, N. Hontama, Y. Inokuchi, T. Haino, E. Aprà, S.S. Xantheas, Phys. Chem. Chem. Phys. 12 (2010) 4569.
- [10] S. Kaneko, Y. Inokuchi, T. Ebata, E. Aprà, S.S. Xantheas, J. Phys. Chem. A 115 (2011) 10846.
- [11] S.-K. Kook, Bull. Korean Chem. Soc. 23 (2002) 1111.
- [12] A. Wei, Chem. Commun. (2006) 1581.
- [13] S.J. Dalgarino, P.K. Thallapally, L.J. Barbour, J.L. Atwood, Chem. Soc. Rev. 36 (2007) 236.
- [14] D.M. Rudkevich, Calixarenes-based nanomaterials, in: J. Vincens, J. Harrowfield (Eds.), *Calixarenes in the Nanoworld*, Springer, Dordrecht, 2007, Chapter 8.
- [15] B. Mokhtari, K. Pourabdollah, N. Dalali, J. Coord. Chem. 64 (2011) 743.
- [16] R. Ludwig, Microchim. Acta 152 (2005) 1.
- [17] R. Zadmid, T. Schrader, Angew. Chem. Int. Ed. Engl. 45 (2006) 2703.
- [18] J.W. Caldwell, P.A. Kollman, J. Am. Chem. Soc. 117 (1995) 4177.
- [19] J.C. Ma, D.A. Dougherty, Chem. Rev. 97 (1997) 1303.
- [20] R. Bernardino, B.J.C. Cabral, Supramol. Chem. 14 (2002) 57.
- [21] J. Vacek, P. Hobza, Int. J. Quantum Chem. 57 (1996) 551.
- [22] R.J. Bernardino, B.J.C. Cabral, J. Phys. Chem. 103 (1999) 9080.
- [23] E.B. Brouwer, G.D. Enright, J.A. Ripmeester, Chem. Commun. (1997) 939.
- [24] D.M. Rudkevich, Eur. J. Org. Chem. 2007 (2007) 3255.
- [25] S. Alavi, J.A. Ripmeester, Chemistry 14 (2008) 1965.
- [26] S. Alavi, T.K. Woo, A. Sirjoosinhg, S. Lang, I. Moudrakovski, J.A. Ripmeester, Chemistry 16 (2010) 11689.
- [27] S. Grimme, J. Comput. Chem. 27 (2006) 1787.
- [28] S. Grimme, J. Antony, S. Ehrlich, H. Krieg, J. Chem. Phys. 132 (2010) 154104.
- [29] T. Risthaus, S. Grimme, J. Chem. Theory Comput. 9 (2013) 1580.
- [30] D. Marx, J. Hutter, *Ab initio molecular dynamics: basic theory and advanced methods*, Cambridge University Press, Cambridge, 2009.
- [31] C. Fiolhais, F. Nogueira, M.A.L. Marques, *A Primer in Density Functional Theory*, Springer-Verlag, Berlin Heidelberg, 2003.
- [32] J. VandeVondele, M. Krack, F. Mohamed, M. Parrinello, T. Chassaing, J. Hutter, Comput. Phys. Commun. 167 (2005) 103.
- [33] G. Lippert, J. Hutter, M. Parrinello, Mol. Phys. 92 (1997) 477.
- [34] S. Goedecker, M. Teter, J. Hutter, Phys. Rev. B 54 (1996) 1703.
- [35] J.P. Perdew, K. Burke, M. Ernzerhof, Phys. Rev. Lett. 77 (1996) 3865.
- [36] G.J. Martyna, M.E. Tuckerman, J. Chem. Phys. 110 (1999) 2810.
- [37] G. Bussi, D. Donadio, M. Parrinello, J. Chem. Phys. 126 (2007) 014101.
- [38] F. Neese, WIREs Comput. Mol. Sci. 2 (2012) 73.
- [39] A. Schafer, C. Huber, R. Ahlrichs, J. Chem. Phys. 100 (1994) 5829.
- [40] C.D. Gutsche, L.J. Bauer, J. Am. Chem. Soc. 107 (1985) 6052.
- [41] P.D.J. Grootenhuis, et al., J. Am. Chem. Soc. 112 (1990) 4165.
- [42] R.A. Aziz, J. Chem. Phys. 99 (1993) 4518.
- [43] D. Roy, M. Marianski, N.T. Maitra, J.J. Dannenberg, J. Chem. Phys. 137 (2012) 134109.
- [44] B.H. Boo, J. Korean Phys. Soc. 57 (2010) 339.
- [45] F. Huang, J. Yang, A. Hao, X. Wu, R. Liu, Q. Ma, Spectrochim. Acta A: Mol. Biomol. Spectrosc. 57 (2001) 1025.
- [46] L.C. Groenen, E. Steinwender, B.T.G. Lutz, J.H. van der Maas, D.N. Reinhoudt, J. Chem. Soc. Perkin Trans. 2 (1992) 1893.
- [47] J. Lang, V. Deckerova, V. Holešovickach, J. Černek, P. Lhoták, J. Chem. Phys. 122 (2005) 044506.
- [48] B.J.C. Cabral, K. Coutinho, S. Canuto, J. Chem. Phys. 138 (2013) 225102.
- [49] V.I. Kovalenko, et al., Russ. Chem. Bull. 51 (2002) 825.